AIAA JOURNAL
Vol. 44, No. 10, October 2006

Reynolds Stress Transport Modeling for High-Lift Airfoil Flows

Bruno Chaouat*
ONERA, 92322 Châtillon, France

DOI: 10.2514/1.21228

Numerical predictions of high-lift airfoil flows are performed on refined grids using a Reynolds stress model that is a variant of Launder and Shima model [Launder, B. E., and Shima, N., "Second Moment Closure for the Near Wall Sublayer: Development and Application," *AIAA Journal*, Vol. 2710, 1989, pp. 1319–1325.] and a standard $k-\epsilon$ model. In this study, the test case of the turbulent flow over the A-airfoil designed by Aérospatiale is considered. Three incidence angles 7.2, 13.3, and 15.3 deg, which correspond to attached and separated flows, are examined for analyzing the performances of the Reynolds stress turbulence model. In particular, emphasis is put on the case 13.3 deg near the static stall which constitutes a challenging test in turbulence modeling since the flow presents complex physics such as a laminar separation bubble, a turbulent reattachment, and a turbulent separation near the trailing edge. Comprehensive comparisons with wind tunnel experiments for the lift and drag coefficients, the pressure and skin friction distributions, as well as the computed velocity, and Reynolds stress turbulent profiles, are worked out. Special attention is devoted to the evolving profiles of the velocity and the turbulent stresses in the boundary layer at six locations on the suction side of the airfoil for incidence angles 7.2 and 13.3 deg. As a result of interest, it is found that the Reynolds stress model predicts both attached and separated flows in a very good agreement with the experimental data. As expected, the $k-\epsilon$ model reveals very poor performance near the static stall.

Introduction

NUMERICAL predictions of flows past airfoils are often used in the aerodynamic design optimization of aircraft wings. For high incidence angles, these flows are of complex physics. They are characterized by strong effects of streamline curvature, adverse pressure gradient caused by the airfoil suction side, flow recirculation, and transition with attached and separated turbulent boundary layers. Separation of flows from the suction side is of major importance. When separation occurs, the turbulence structure is affected within the boundary layer and leads to dramatic loss of lift and rise in drag. For engineering applications, airfoil flows are generally performed by solving the Reynolds averaged Navier–Stokes equations (RANS) using viscosity models such as the Baldwin-Lomax model [1], the Spalart–Allmaras model [2], or two-equation turbulence models [3,4]. These algebraic or first-order closure models perform well for shear flows in which the shear stress is the only dynamically important component of the stress tensor [5]. But for high-lift flows subjected to high curvature walls involving separation and recirculation, the normal stresses also play an important role in the determining of the flow structures.

A reliable prediction of normal turbulent stresses is required for aeronautical applications. Obviously, simple turbulence models based on the Boussinesq hypothesis erroneously produce normal stresses because of the simple linkage between the stresses and strain components which fails to represent the difference in directional alignment between the principal stresses and strains. To overcome the deficiencies of the Boussinesq hypothesis, nonlinear algebraic stress models have been developed and applied recently in the framework of multi-element airfoils [6] with improvement in the prediction of turbulent shear stress behind the trailing edge. In contrast to first-order closure models, second-order closure models [7,8] based on the transport equation of each individual Reynolds stress components contain more physics. Because of their formulation, they are able to take into account the basic interaction between the shear stress, the normal stress anisotropy, and the geometry curvature. Indeed, exact production terms that appear as source or sink in the transport equations for each individual Reynolds stress component are expressed by the tensorial product of the Reynolds stresses by the mean velocity gradients which depend on the geometry curvature. So, these models are much more sensitized to the curvature than first-order models which take into account only the production of the turbulent kinetic energy as discussed in detail by Leschziner [9] for the particular example of a boundary layer on a convex wall. The main characteristic of second-order closure models lies on the pressure-strain correlation which is of major importance. This term incorporates history and nonlocal effects of the flows. It is composed of slow and rapid parts that are able to reproduce the flow anisotropy and redistribute the turbulent kinetic energy among the Reynolds stress components. The pressure-strain term has been modeled in the past, assuming homogeneous flows that are near equilibrium [7] and recent developments in this direction have been made using invariance tensorial approach [10]. For calculation of complex wall-bounded turbulent flows, a wall reflection term is generally incorporated in the model to account for the surface contribution from the solution of the Poisson equation [11,12]. This term is useful for reproducing the logarithmic region of the turbulent boundary layer. New Reynolds stress models (RSM) also were recently developed with echo-free closures [13] or with inhomogeneity approaches [14,15] for avoiding wall treatments in complex geometries.

Although second-order closure models account for more physics than first-order closure models, their capacities in predicting flow separations are not warranted and must be examined for each case. Usually, standard first-order closure models fail to predict the separation for high incidence angles because of the excessive level of the shear stress returned by these models in boundary layer with adverse pressure gradient [3,16]. For aerodynamic applications, shortcomings of these models were overcome using the SST (shear stress transport) correction proposed by Menter [17,18] based on the Bradshaw relation between the shear stress and the turbulent kinetic energy. This correction consists in limiting the eddy-viscosity in presence of adverse pressure gradient flow to improve flow separation. When the modeling increases from one-equation models to full Reynolds stress closure, the predictive tendency of flow separation progressively improves [16]. However, prediction of a massive separation requires generally specific modifications as

---

Received 17 November 2005; revision received 17 March 2006; accepted for publication 11 April 2006. Copyright © 2006 by the American Institute of Aeronautics and Astronautics, Inc. All rights reserved. Copies of this paper may be made for personal or internal use, on condition that the copier pay the $10.00 per-copy fee to the Copyright Clearance Center, Inc., 222 Rosewood Drive, Danvers, MA 01923; include the code $10.00 in correspondence with the CCC.

*Senior Scientist, Department of Computational Fluid Dynamics. Member AIAA.

mentioned by Haase in the European computational aerodynamics research project (ECARP) [16].

Leaving the eddy-viscosity hypothesis in favor of solving the transport equations for the individual Reynolds stresses is certainly a more universal approach. In that framework, second-order closure models remain a good compromise between viscosity models and large eddy simulations [19,20] that require very large computing time, although recent progress based on new, partially integrated transport models are made to render large eddy simulations more suitable to engineering applications [21–23]. Despite their advantages, second-moment closures are, however, not widely used in a general way for aerodynamics applications because of the increased mathematical complexity arising from nonlinearity and interequation coupling [24]. These issues in turbulence modeling for aeronautical applications are discussed in detail by Leschziner [25] from both physical and numerical points of view.

The present study investigates the predictive performances of a variant Reynolds stress model of Launder and Shima [26] for high-lift airfoil flows. Computations using the $k-\epsilon$ model of Launder and Sharma [27] based on the Boussinesq hypothesis are also performed, especially for comparing the turbulent stresses with emphasis on flow anisotropy. The aerodynamics application of the turbulent flow past the A-airfoil designed by Aérospatiale, subjected to a large range of incidence that includes the static stall, is considered. The flow around this airfoil lift is one of the most difficult computational tests due to the extreme sensitivity of boundary layer separation to geometric and turbulence parameters. Special attention is therefore devoted to the flow separation, the evolving velocities, and the turbulent stresses in the boundary layer at several locations on the suction side.

Governing Equations

Turbulent flow of a viscous fluid is considered. As in the usual treatments of turbulence, the flow variable ξ is decomposed into ensemble Reynolds mean and fluctuating parts as $\xi = \bar{\xi} + \xi'$. In the present case, the Favre average is used for compressible fluid so that the variable ξ can be written as $\xi = \tilde{\xi} + \xi''$ with the particular properties $\tilde{\xi''} = 0$ and $\overline{\rho\xi''} = 0$ where ρ is the mass density. These relations imply that $\tilde{\xi} = \overline{\rho\xi}/\bar{\rho}$. The ensemble average of the Navier–Stokes equations produces in Favre variables the following form of the mass, momentum, and energy equations

$$\frac{\partial\bar{\rho}}{\partial t} + \frac{\partial}{\partial x_j}(\bar{\rho}\tilde{u}_j) = 0 \tag{1}$$

$$\frac{\partial}{\partial t}(\bar{\rho}\,\tilde{u}_i) + \frac{\partial}{\partial x_j}(\bar{\rho}\tilde{u}_i\tilde{u}_j) = \frac{\partial\bar{\Sigma}_{ij}}{\partial x_j} \tag{2}$$

$$\begin{aligned}\frac{\partial}{\partial t}(\bar{\rho}\tilde{E}) + \frac{\partial}{\partial x_j}(\bar{\rho}\tilde{E}\,\tilde{u}_j) = \frac{\partial}{\partial x_j}(\bar{\Sigma}_{ij}\tilde{u}_i) + \frac{\partial}{\partial x_j}\left(\overline{\sigma_{ij}u_i''} - \frac{1}{2}\bar{\rho}\,\widetilde{u_k''u_k''u_j''}\right)\\ -\frac{\partial\bar{q}_j}{\partial x_j}\end{aligned} \tag{3}$$

where u_i, E, Σ_{ij}, σ_{ij}, and q_i are the velocity vector, the total energy, the total stress tensor, the viscous stress tensor, and the total heat flux vector, respectively. The mean stress tensor $\bar{\Sigma}_{ij}$ is composed by the mean pressure $\bar{p}$, the mean viscous stress $\bar{\sigma}_{ij}$, and the turbulent stress $\bar{\rho}\tau_{ij}$ as follows

$$\bar{\Sigma}_{ij} = -\bar{p}\delta_{ij} + \bar{\sigma}_{ij} - \bar{\rho}\tau_{ij} \tag{4}$$

In this expression, the viscous tensor $\bar{\sigma}_{ij}$ takes the usual form

$$\bar{\sigma}_{ij} = \bar{\mu}\left(\frac{\partial\bar{u}_i}{\partial x_j} + \frac{\partial\bar{u}_j}{\partial x_i}\right) - \frac{2}{3}\bar{\mu}\frac{\partial\bar{u}_k}{\partial x_k}\delta_{ij} \tag{5}$$

where μ is the molecular viscosity. The Favre-averaged Reynolds stress tensor τ_{ij} is defined by $\tau_{ij} = \widetilde{u_i''u_j''}$. Assuming ideal gas law, the mean thermodynamic pressure is computed by

$$\bar{p} = (\gamma - 1)\bar{\rho}\left(\tilde{E} - \frac{1}{2}\tilde{u}_i\tilde{u}_i - \frac{1}{2}\tau_{ii}\right) \tag{6}$$

where γ is the ratio of specific heats. The presence of the turbulent contribution τ_{ii} in Eq. (6) shows a coupling between the mean equations and the turbulent transport equations. The mean heat flux $\bar{q}_i$ is composed of the laminar and turbulent flux contributions

$$\bar{q}_i = -\bar{\kappa}\frac{\partial\bar{T}}{\partial x_i} + \bar{\rho}\,\widetilde{h''u_i''} \tag{7}$$

where T, h, and κ are the temperature, the specific enthalpy, and the thermal conductivity, respectively. Closure of the mean flow equations is necessary for the turbulent stress $\bar{\rho}\,\widetilde{u_i''u_j''}$, the molecular diffusion $\overline{\sigma_{ij}u_i''}$, the turbulent transport $\bar{\rho}\,\widetilde{u_k''u_k''u_j''}$, and the turbulent heat flux $\bar{\rho}\,\widetilde{h''u_i''}$.

Turbulence Model

Reynolds Stress Transport Equation

The Favre-averaged correlation tensor $\tau_{ij} = \widetilde{u_i''u_j''}$ is computed by means of a variant Reynolds stress model of Launder and Shima [26]. This model has been selected because it embodies some advanced concepts such as the invariant functions for approaching walls and contains only a few empirical terms. Thus, it is a good candidate to handle a large variety of flows. It ensures computational robustness and satisfactory performances in many wall-bounded flows [28]. In this work, relative to its original form, some modifications are proposed for improving the airfoil flow predictions. The modeled transport equation of the Reynolds stress tensor extended to compressible flows can be written as

$$\begin{aligned}\frac{\partial}{\partial t}(\bar{\rho}\tau_{ij}) + \frac{\partial}{\partial x_k}(\bar{\rho}\tau_{ij}\tilde{u}_k) = P_{ij} - \frac{2}{3}\bar{\rho}\epsilon\delta_{ij} + \Phi_{ij1} + \Phi_{ij2}\\ + \Phi_{ijw} + J_{ij}\end{aligned} \tag{8}$$

where the terms on the right-hand side of Eq. (8) are identified as production by the mean flow, dissipation, slow redistribution, rapid redistribution, wall reflection, and diffusion, respectively. The production term takes the exact expression

$$P_{ij} = -\bar{\rho}\tau_{ik}\frac{\partial\tilde{u}_j}{\partial x_k} - \bar{\rho}\tau_{jk}\frac{\partial\tilde{u}_i}{\partial x_k} \tag{9}$$

The slow and rapid redistribution terms composed by the pressure-strain correlations are modeled by the term of Rotta which governs the return to isotropy

$$\Phi_{ij1} = -c_1\bar{\rho}\epsilon a_{ij} \tag{10}$$

where, in this expression

$$a_{ij} = \frac{\tau_{ij} - (2/3)k\delta_{ij}}{k}$$

is the anisotropic tensor, and by the term of the isotropization of production

$$\Phi_{ij2} = -c_2\left(P_{ij} - \frac{1}{3}P_{kk}\delta_{ij}\right) \tag{11}$$

The turbulent kinetic energy is denoted $k = \tau_{mm}/2$. In the Launder and Shima model, the anisotropic part of the dissipation tensor $\epsilon_{ij} - 2/3\delta_{ij}\epsilon$ is modeled in the slow and rapid redistribution terms. Other models are developed with the anisotropy of the dissipation tensor [29]. The reflection term ϕ_{ijw} is based on the work of Gibson and Launder [11]

$$\Phi_{ijw} = c_{1w}\frac{\bar{\rho}\epsilon}{k}\left(\tau_{kl}n_k n_l\delta_{ij} - \frac{3}{2}\tau_{ki}n_k n_j - \frac{3}{2}\tau_{kj}n_k n_i\right)f_w + c_{2w}\left(\Phi_{kl2}n_k n_l\delta_{ij} - \frac{3}{2}\Phi_{ik2}n_k n_j - \frac{3}{2}\Phi_{jk2}n_k n_i\right)f_w \tag{12}$$

where n is the unit vector normal to the wall and f_w is a damping function of the wall distance. In Eq. (12), the quantities c_1, c_2, c_{1w}, and c_{2w} are some functions which depend on the second and third invariants $A_2 = a_{ij}a_{ji}$, $A_3 = a_{ij}a_{jk}a_{ki}$, the flatness coefficient parameter $A = 1 - \frac{9}{8}(A_2 - A_3)$, and the turbulent Reynolds number $Re_t = k^2/\nu\epsilon$. The flatness parameter varies continuously between zero in two-component turbulence limit and unity for isotropic turbulence. Regarding the model of Launder and Shima [26], the function c_2 in Eq. (11) is modified to satisfy the exact equation of the pressure-strain correlation for the limit of isotropic turbulence [30] given by

$$\Phi_{ij2} = \frac{2}{5}\bar{\rho}k\left(\frac{\partial\tilde{u}_i}{\partial x_j} + \frac{\partial\tilde{u}_j}{\partial x_i}\right) \tag{13}$$

To do that, we suggest the function $c_2 = 0.6A^{1/2}$ instead of the original function $c_2 = 0.75A^{1/2}$. The diffusion term is conventionally approximated by the generalized gradient-diffusion hypothesis proposed by Daly and Harlow [31]

$$J_{ij} = \frac{\partial}{\partial x_k}\left(\bar{\mu}\frac{\partial\tau_{ij}}{\partial x_k} + c_s\bar{\rho}\frac{k}{\epsilon}\tau_{kl}\frac{\partial\tau_{ij}}{\partial x_l}\right) \tag{14}$$

where the coefficient c_s is set to 0.22.

Dissipation Rate Transport Equation

The dissipation rate ϵ, which appears in Eq. (8), is computed by means of the modeled transport equation which has been modified in regard to its original form [26]. We propose the equation

$$\frac{\partial}{\partial t}(\bar{\rho}\epsilon) + \frac{\partial}{\partial x_j}(\bar{\rho}\tilde{u}_j\epsilon) = (c_{\epsilon_1} + \psi_1)\overline{\rho}\frac{\epsilon}{2k}P_{mm} - c_{\epsilon_2}f_\epsilon\bar{\rho}\frac{\tilde{\epsilon}\epsilon}{k} + E_\epsilon + J_\epsilon \tag{15}$$

where $\tilde{\epsilon} = \epsilon - 2\nu(\partial\sqrt{k}/\partial x_n)^2$ and x_n is the normal coordinate to the wall. In Eq. (15), the first term of the right-hand side represents the production, whereas the second term is the destruction of the dissipation rate. Relative to its original form, a new term involving the second derivative of the mean velocity

$$E_\epsilon = c_{\epsilon_3}\mu\frac{k}{\epsilon}\tau_{kl}\frac{\partial^2\tilde{u}_i}{\partial x_k\partial x_j}\frac{\partial^2\tilde{u}_i}{\partial x_l\partial x_j} \tag{16}$$

is first added in the right-hand side of Eq. (15) for properly capturing the aerodynamic velocity wall layer. This term can be regarded as the outcome of using the generalized gradient-diffusion hypothesis to close a term $\partial^2\tilde{u}_i/\partial x_k\partial x_j$ in the exact ϵ equation [32]. Secondly, a new function f_ϵ depending on the Reynolds number is introduced in the destruction term for giving the desired limiting values of the decay exponents [33]. Finally, the original term ψ_1 sensitized to the ratio of turbulence production to dissipation rate in the Launder and Shima model [26] defined by

$$\psi_1 = 1.5A\left(\frac{P_{mm}}{2\bar{\rho}\epsilon} - 1\right) \tag{17}$$

Table 1 Functions used in the RSM model

Functions	Expressions
c_1	$1 + 2.58AA_2^{1/2}\{1 - \exp[-(Re_t/150)^2]\}$
c_2	$0.6A^{\frac{1}{2}}$
c_{1w}	$(-2/3)c_1 + (5/3)$
c_{2w}	$\max[(2/3)c_2 - (1/6), 0]/c_2$
f_w	$0.4k^{3/2}/\epsilon x_2$
f_ϵ	$1 - 0.22\exp[-(Re_t/6)^2]$

has been bounded to prevent early laminarization when flows are far from equilibrium [34]. To do that, we impose the condition $|\psi_1| \leq c_{\epsilon_2} - c_{\epsilon_1}$ for limiting the production of the dissipation rate $(c_{\epsilon_1} + \psi_1)\overline{\rho}\epsilon P_{mm}/2k$ in regard to the destruction of the dissipation rate $c_{\epsilon_2}\bar{\rho}f_\epsilon\tilde{\epsilon}\epsilon/k$. This condition has a local character and was found particularly useful in reproducing the influence and flow pattern around separation and reattachment. It has been also verified that this condition has no effects for standard flows close to equilibrium where production approaches dissipation. Moreover, Eq. (15) also differs from the original equation of Launder and Shima [26] through the function $\psi_2 = 0.3(1 - 0.3A_2)\exp[-(0.002Re_t)^2]$ which has been reduced to zero because of its empirical form which alters the *basic* formulation of the dissipation rate equation. Note that other authors [35] using the Launder and Shima model [26] have also modified this equation in a different way. The diffusion term J_ϵ is modeled assuming gradient-diffusion hypothesis

$$J_\epsilon = \frac{\partial}{\partial x_i}\left(\bar{\mu}\frac{\partial\epsilon}{\partial x_i} + c_\epsilon\bar{\rho}\frac{k}{\epsilon}\tau_{ij}\frac{\partial\epsilon}{\partial x_j}\right) \tag{18}$$

where the coefficient c_ϵ is set to 0.18. Values of the constant coefficients are $c_{\epsilon_1} = 1.45$, $c_{\epsilon_2} = 1.9$. The computation of the fully turbulent channel flow leads the optimized value of the coefficient $c_{\epsilon_3} = 0.10$. The functions used in this model are listed in Table 1.

Turbulent Heat Flux and Diffusive Terms

The velocity-enthalpy correlations $\widetilde{h''u_i''}$ appearing in the total-energy equation is computed by means of k and ϵ variables

$$\widetilde{h''u_i''} = -\frac{c_\mu k^2}{\epsilon}\frac{c_p}{P_{r_t}}\frac{\partial\tilde{T}}{\partial x_i} \tag{19}$$

where c_p and P_{r_t} are the specific heat at constant pressure and the turbulent Prandtl number, respectively. The diffusive terms are modeled by a gradient hypothesis

$$\overline{\sigma_{ij}u_i''} - \frac{1}{2}\bar{\rho}\,\widetilde{u_k''u_k''u_j''} = \left(\bar{\mu}\delta_{jm} + c_s\bar{\rho}\frac{k}{\epsilon}\tau_{jm}\right)\frac{\partial k}{\partial x_m} \tag{20}$$

Realizability Conditions

In second-order closure turbulence modeling, it is essential to check if the RSM model is able to satisfy the realizability conditions to ensure positive normal stress computations. Because of these complex conditions [36] which impose nonnegative values of the three-principal invariants I_i in the characteristic polynomial $P(\lambda) = \lambda^3 - I_1\lambda^2 + I_2\lambda - I_3$ of the matrix formed by the components τ_{ij}, we prefer to examine the weak form of realizability [36]. This equation requires that, when a principal Reynolds stress component vanishes, its time derivative must be positive. This new condition also ensures that a negative energy component cannot occur when this constraint is satisfied. The modeled transport Eq. (8) of the turbulent stress component $\tau_{\alpha\alpha}$ can be written in the principal axis [37] as

$$\frac{\partial}{\partial t}(\bar{\rho}\tau_{\alpha\alpha}) + \frac{\partial}{\partial x_\beta}(\bar{\rho}\tilde{u}_\beta\tau_{\alpha\alpha}) = P_{\alpha\alpha} - \frac{2}{3}\bar{\rho}\epsilon - c_1\bar{\rho}\frac{\epsilon}{k}\left(\tau_{\alpha\alpha} - \frac{2}{3}k\right) - c_2\left(P_{\alpha\alpha} - \frac{1}{3}P_{\beta\beta}\right) \tag{21}$$

where in that equation, only the index β is contracted. The diffusion term as well as the reflection term are not considered in Eq. (21). When the component stress $\tau_{\alpha\alpha}$ vanishes, it can be shown that the production term $P_{\alpha\alpha}$ is zero so that the weak realizability conditions imply

$$c_1 \geq 1 - c_2\frac{P_{\beta\beta}}{2\bar{\rho}\epsilon} \tag{22}$$

Because of the expressions of the coefficients c_1 and c_2, Eq. (22) is verified when the production term $P_{\beta\beta}/2$ of the turbulent kinetic energy is positive. This corresponds to the usual case of flow physics and ensures therefore the satisfaction of the weak realizability constraint.

Numerical Approach

The finite volume technique is adopted in the research code developed by Chaouat [38] to solve the full transport equations of compressible fluids. Considering the staggered grid cell around the point (i, j), the variation of the averaged unknown U on the control volume $v(\Omega)$ is obtained by the following conservation equation

$$\frac{\partial U}{\partial t} = -\frac{1}{v(\Omega)} \sum_{\sigma} (F_k - F_{vk}) \otimes n_{\sigma k} A_\sigma + S \tag{23}$$

where F_k and F_{vk} represent, respectively, the convective and viscous fluxes through the surfaces A_σ around the control volume $v(\Omega)$, n_σ is the unit normal to the surface A_σ and S is the source term. The expressions of the quantities U, F_k, F_{vk} and S written in compact form are

$$U = \begin{bmatrix} \bar\rho \\ \bar\rho\tilde u_i \\ \bar\rho\,\tilde E \\ \bar\rho\tau_{ij} \\ \bar\rho\epsilon \end{bmatrix}, \qquad F_k = \begin{bmatrix} \bar\rho\tilde u_k \\ \bar\rho\tilde u_i\tilde u_k \\ \bar\rho\,\tilde E\,\tilde u_k \\ \bar\rho\tau_{ij}\tilde u_k \\ \bar\rho\epsilon\tilde u_k \end{bmatrix},$$

$$F_{vk} = \begin{bmatrix} 0 \\ \bar\Sigma_{ik} \\ \bar\Sigma_{km}\tilde u_m - \bar q_k + c_s\bar\rho\frac{k}{\epsilon}\tau_{km}\frac{\partial k}{\partial x_m} \\ \mu\frac{\partial \tau_{ij}}{\partial x_k} + c_s\bar\rho\frac{k}{\epsilon}\tau_{km}\frac{\partial \tau_{ij}}{\partial x_m} \\ \mu\frac{\partial \epsilon}{\partial x_k} + c_\epsilon\bar\rho\frac{k}{\epsilon}\tau_{km}\frac{\partial \epsilon}{\partial x_m} \end{bmatrix},$$

$$S = \begin{bmatrix} 0 \\ 0 \\ 0 \\ P_{ij} + \Phi_{ij1} + \Phi_{ij2} + \Phi_{ijw} - \frac{2}{3}\bar\rho\delta_{ij}\epsilon \\ (c_{\epsilon_1} + \psi_1)\frac{\epsilon}{2k}P_{mm} - c_{\epsilon_2}\bar\rho f_\epsilon\frac{\epsilon\tilde\epsilon}{k} + E_\epsilon \end{bmatrix}$$

In a developed form, the vector U is of dimension 11 for a two-dimensional computation. The vector U is evaluated at the center of each cell whereas the convective flux F at the cell interfaces is computed by means of an approximate Riemann solver as follows [39]

$$F = \frac{F(U_R) + F(U_L)}{2} - |J|\left(\frac{U_R - U_L}{2}\right) \tag{24}$$

where $|J|$ is the absolute Jacobian matrix evaluated at the interface and U_R, U_L are the two evaluations of the vector U at the right and left side of the interface. This matrix is determined using a formal decomposition of operators introduced by Dutoya and Errera [40]. In this work, we have extended their theory to the turbulent variables τ_{ij} and ϵ and we found that the absolute Jacobian matrix can be expressed very simply as a function of the identity matrix and two tensor products by the relation:

$$|J| = |\lambda^0| I + [|\lambda^+| - |\lambda^0|] r_+ \otimes l^+ + [|\lambda^-| - |\lambda^0|] r_- \otimes l^- \tag{25}$$

with the following definitions for the vectors r_+, r_-, l^+ and l^-

$$r_+ = \begin{bmatrix} 1 \\ \tilde u_i + c n_{\sigma i} \\ \tilde H + c\tilde u_m n_{\sigma m} \\ \tau_{ij} \\ \epsilon \end{bmatrix}, \qquad r_- = \begin{bmatrix} 1 \\ \tilde u_i - c n_{\sigma i} \\ \tilde H - c\tilde u_m n_{\sigma m} \\ \tau_{ij} \\ \epsilon \end{bmatrix}$$

$$l^+ = \frac{1}{2c}\left[\frac{(\gamma-1)k}{c} - \tilde u_m n_{\sigma m}, -\frac{(\gamma-1)\tilde u_i}{c} + n_{\sigma i}, \frac{\gamma-1}{c}, \frac{-(\gamma-1)\delta_{ij}}{2c}, 0\right] \tag{26}$$

$$l^- = \frac{1}{2c}\left[\frac{(\gamma-1)k}{c} + \tilde u_m n_{\sigma m}, -\frac{(\gamma-1)\tilde u_i}{c} - n_{\sigma i}, \frac{\gamma-1}{c}, \frac{-(\gamma-1)\delta_{ij}}{2c}, 0\right] \tag{27}$$

In these expressions, n_σ is the normal vector to the surface A_σ, I is the identity matrix, c is the velocity of sound, $\lambda^+ = u_j n_{\sigma j} + c$, $\lambda^- = u_j n_{\sigma j} - c$, and $\lambda^0 = u_j n_{\sigma j}$ are the eigenvalues, and H denotes the total enthalpy. Equation (25) is of practical interest for evaluating the function $|J(U)|$ in an efficient way that requires less addition and multiplication than a conventional algorithm [40]. Indeed, from the mathematical relation $[a \otimes b]U = a(b \cdot U)$ where a and b are vectors, the function $|J|(U)$ can be computed as follows:

$$|J|(U) = |\lambda^0|(U) + [|\lambda^+| - |\lambda^0|] r_+ (l^+ \cdot U) + [|\lambda^-| - |\lambda^0|] r_- (l^- \cdot U) \tag{28}$$

where the quantities $(l^+ \cdot U)$ and $(l^- \cdot U)$ denote two scalar products. Therefore, relation (28) avoids the explicit tensorial computations of the operators $(r_+ \otimes l^+)U$ and $(r_- \otimes l^-)U$. The two approximations U_R and U_L for the right and left sides in Eq. (24) are evaluated on each interface of the mesh using a MUSCL approach that requires five points. To obtain a monotonicity solution, the variable $U^L_{i-\frac{1}{2},j}$ on the left side of the interface $i - \frac{1}{2}$, j is computed by means of the relation

$$U^L_{i-\frac{1}{2},j} = \Phi^L_{i,j} U^{L*}_{i-\frac{1}{2},j} + (1 - \Phi^L_{i,j}) U^C_{i-\frac{1}{2},j} \tag{29}$$

where the variables $U^{L*}_{i-\frac{1}{2},j}$ and $U^C_{i-\frac{1}{2},j}$ are evaluated by an interpolation

$$U^{L*}_{i-\frac{1}{2},j} = \frac{-\delta x_{i-1,j} U_{i-2,j} + (\delta x_{i-2,j} + 2\delta x_{i-1,j}) U_{i-1,j}}{\delta x_{i-2,j} + \delta x_{i-1,j}} \tag{30}$$

and

$$U^C_{i-\frac{1}{2},j} = \frac{\delta x_{i,j} U_{i-1,j} + \delta x_{i-1,j} U_{i,j}}{\delta x_{i-1,j} + \delta x_{i,j}} \tag{31}$$

where the quantity $\delta x_{i,j} = x_1(i + \frac{1}{2}, j) - x_1(i - \frac{1}{2}, j)$ denotes the spatial increment. In Eq. (29), $\Phi^L_{i,j}$ is the flux limiter defined by

$$\Phi^L_{i,j} = \frac{x^L_A |U_{i,j} - U_{i-1,j}|}{x^L_A |U_{i,j} - U_{i-1,j}| + x^L_B |U_{i-1,j} - U_{i-2,j}|} \tag{32}$$

with

$$x^L_A = \frac{\delta x_{i-1,j}}{\delta x_{i-1,j} + \delta x_{i,j}} \tag{33}$$

and

$$x^L_B = \frac{\delta x_{i-1,j}}{\delta x_{i-2,j} + \delta x_{i-1,j}} \tag{34}$$

The variables $U^{L*}_{i-\frac{1}{2},j}$ and $U^C_{i-\frac{1}{2},j}$ are expressed in terms of the variables $U_{i,j}$, $U_{i-1,j}$, and $U_{i-2,j}$ to obtain a numerical scheme of second-order accuracy in space discretization. Because of the flux limiter, this scheme evolves from a second-order centered scheme where $\Phi^L_{i,j} = 0$, to a second-order upwind scheme where $\Phi^L_{i,j} = 1$. The centered scheme is applied with the aim to minimize the dissipative and dispersive numerical errors. In addition, the upwind scheme is used for suppressing the spurious discontinuities. In the smooth region of the flow, the flux limiter is close to zero except for the points or region with sharp extrema in the variation of U. As usual, the viscous fluxes are computed using a second-order centered space discretization. The source terms of the turbulence model are linearized to avoid numerical instabilities. The governing equations are integrated in time using a three-stage Runge–Kutta method. These combined space-time methods enable one to obtain a total variation diminishing (TVD) scheme of high resolution that ensures monotonicity solutions. The present numerical scheme is therefore relevant for computing aeronautical applications involving separated flows using a Reynolds stress model [28,41].

Test Case and Experiment

The Aérospatial A-airfoil subjected to a large range of incidence angles that includes the static stall is considered. The Reynolds number, based on the upstream velocity $u_\infty = 51\ \mathrm{ms}^{-1}$ and the chord $c = 0.6$ m, is equal to 2.1×10^6. The upstream Mach number takes the value $M_\infty = 0.15$. Such conditions are fairly realistic for aeronautical flows. In the past, this test case was selected in the ECARP project [16] because it constitutes an extreme numerical challenge at 13.3 deg angle of incidence and also because experimental results are available. Experiments have been carried out in two different wind tunnels F1 (1.5 m height × 3.5 m width) and F2 (1.4 × 1.8 m) at ONERA [42,43]. Both wind tunnels F1 and F2 provided global measurements for the lift, drag, and pressure coefficients, but only F2 detailed experimental profiles of the velocity and turbulent stresses in the boundary layer for incidence angles 7.2 and 13.3 deg. The LDV measurements in the F2 wind tunnel indicated that the flow is two-dimensional up to an incidence of 13.3 deg. Because of the larger section of F1 compared with F2, three-dimensional effects appeared in the F1 wind tunnel at higher angle of attack than in the F2 wind tunnel. In these conditions, the lift coefficient is assumed to be quite underestimated in the F2 tunnel for angle of attack greater than 13.3 deg, whereas the drag coefficient is found to be overestimated. That explains some differences between F1 and F2 measurements for the lift and drag coefficients that are attributed to three-dimensional effects [43]. Differences between the two wind tunnels' measurements for the lift and drag coefficients therefore cause little confusion for the numerical comparisons, especially because the experimental investigators stated that the reproducibility of the F2 data have been more carefully obtained than that of the F1 measurements.

In the experiments, the transition on the pressure surface was fixed at 30% of the chord, whereas it was free on the suction side. The experimental observations have revealed that the flow remains attached around the airfoil at $\alpha = 7.2$ deg angle of incidence. But the case at $\alpha = 13.3$ deg is much more complex. The experiment indicated that a transitional bubble, i.e., laminar separation bubble with following transitional reattachment, occurs on the suction side at $x/c = 0.12$. After this position, the turbulent boundary layer subjected to a strong adverse pressure gradient grows until it separates at $x/c \approx 0.82$ creating a small recirculation zone that extends to the trailing edge. Because of that complex physics phenomenon, this flow is much more difficult to predict than a situation involving massive separation at high angle of attack or where separation occurs at a sharp edge.

In the framework of the ECARP project [16], computations using a large variety of different models ranging from algebraic models to second-order closure models were performed to investigate the most promising model with respect to separation and stall prediction. As a result, Haase et al. [16] mentioned that all standard eddy-viscosity transport-equation models failed to predict separation. Application of the SST correction has been demonstrated to improve the solutions of two-equation models in the tendency to separate at moderate angle of attack, but does not guarantee an accurate prediction of stall. Both nonlinear eddy-viscosity and second-moment closure were found superior to the linear eddy-viscosity models, but were also unable to predict the separation at 13.3 deg because of the slightly high level of shear stress returned to the wall. Only modified versions of these models produced a separation behavior. For instance, a drastic reduction of the viscosity coefficient C_μ for the nonlinear eddy-viscosity model was found to give benefits. For the basic RSM model of Launder et al. [7] used in the ECARP project, Lien and Leschziner [44] truncated the term ϕ_{ijw} of the pressure-strain fluctuation correlations to reduce the near-wall shear stress. Although some improvements have been made, this ad hoc modification appears too specific for that type of flow and cannot be applied in a different framework. Another point to mention concerns the grids used in the ECARP project. Because the laminar bubble resolution affects the downstream flow evolution, these grids appear too coarse (177 × 65, 256 × 64, 353 × 65), to obtain grid independent results with the various turbulence models. In these conditions, any firm assessment on these turbulence models was premature because the grid refinement was not sufficient to obtain the grid independent results.

Numerical Results and Discussions

Conditions of Computations

The present numerical computations are performed on different C-grids such as 256 × 97, 513 × 97, and 1025 × 193. Three incidence angles are examined, 7.2, 13.3, and 15.3 deg. Figure 1 shows the computational grid 513 × 97 around the airfoil designed by Aérospatiale. The grids extend 10 chords away from the airfoil to concentrate the points in the vicinity of the airfoil. The refined grid is analytically generated from the grid 513 × 97 by the method of natural cubic spline interpolations requiring the continuities for the first and second derivatives at the interface. The dimensionless distance between the first chordline and the wall is less than 0.5 in wall units. In that condition, the turbulence models can be applied in a low Reynolds number formulation for approaching walls and the grid refinement provides full resolution for the boundary layer. The grid studies are motivated by the necessity of checking numerically the grid independence of the solution as well as the consistency of the turbulence models.

According to the conclusion of Haase [16], the computations are performed with a free transition resolution to assess the performances of the turbulence models. For the cases 13.3 and 15.3 deg, attempts are made to resolve numerically the laminar bubble which is known to influence the transition location of turbulence as well as the separation at the trailing edge. In the present computations, a local time-step technique is used to accelerate convergence to the stationary state. For each computation, convergence of the numerical results is achieved when the average residual profiles go to zero for each dependent variable. The CPU cost per cell and per inner iteration is about 1.5 μs. The computations are performed on a single processor of an NEC-SX5 supercomputer, and the code is running approximately at 4600 mega floating point operations per second. Relative to the $k - \epsilon$ model, RSM computations only require 25% more CPU time. Although the code is well-vectorized, it appears that the convergence towards the steady-state regime is slow. This is mainly caused by the combinations of fine grids and low Mach numbers (Mach ≤ 0.3).

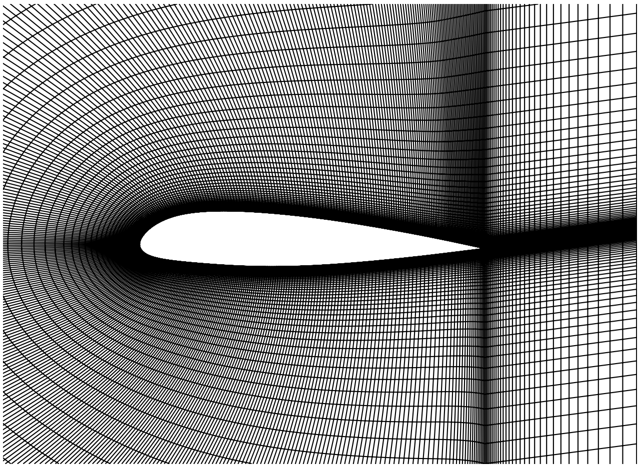

Fig. 1 Computational grid 513 × 97 around the *A*-airfoil designed by Aérospatiale.

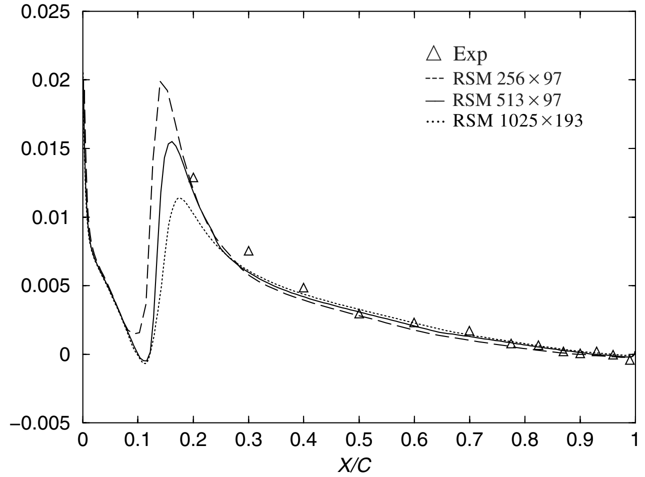

Fig. 2 Effect of grid density. Friction coefficient $C_f = \tau_w/(0.5\rho_\infty u_\infty^2)$ on the suction side; $\alpha = 13.3$ deg.

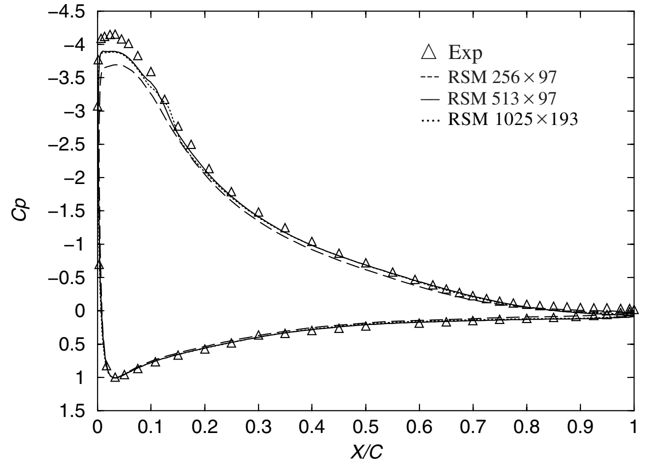

Fig. 3 Effect of grid density. Pressure coefficient $C_p = (p - p_\infty)/(0.5\rho_\infty u_\infty^2)$ around the airfoil; $\alpha = 13.3$ deg.

To check the grid independence solutions, the RSM computational results are presented on different grids for the friction and pressure coefficients. Figures 2 and 3 show the friction and pressure distributions for the *A*-airfoil flow at 13.3 deg angle of incidence which is the case of particular interest. It is found that the friction and pressure distributions computed on the medium and refined grids are practically identical except at and just downstream of the transition, where the friction coefficient differs little. On the contrary, larger deviations in these coefficients appear between the coarse grid and the other grids, indicating that the coarse grid is not appropriate for the *A*-airfoil computations. Other distributions concerning the computational results performed on the medium and refined grids have been examined such as the velocity and turbulent profiles, confirming that these evolutions remain unchanged and that the medium grid is sufficiently dense for valid conclusion. It has been also verified that the global coefficients such as the drag and lift vary only within 1%. The same results have been obtained for other incidence angles. Since the change is negligible between the medium and refined grids, only results associated with the medium grid 513×97 are then presented in the following.

Lift and Drag Coefficients

The evolution of the computed lift coefficient C_L versus the angle of attack α or the drag coefficient C_D are provided, respectively, in Figs. 4 and 5. The results are similar for both turbulence models at incidence angle 7.2 deg. However, at incidence angles 13.3 and 15.3 deg, some differences can be observed. The $k - \epsilon$ results agree better with F1 measurements, whereas the RSM results agree better with F2 measurements. Relative to the $k - \epsilon$ model, the second-order model yields a significant decrease in the lift, indicating that the separations on the suction side occur at 13.3 and 15.3 deg incidence angles.

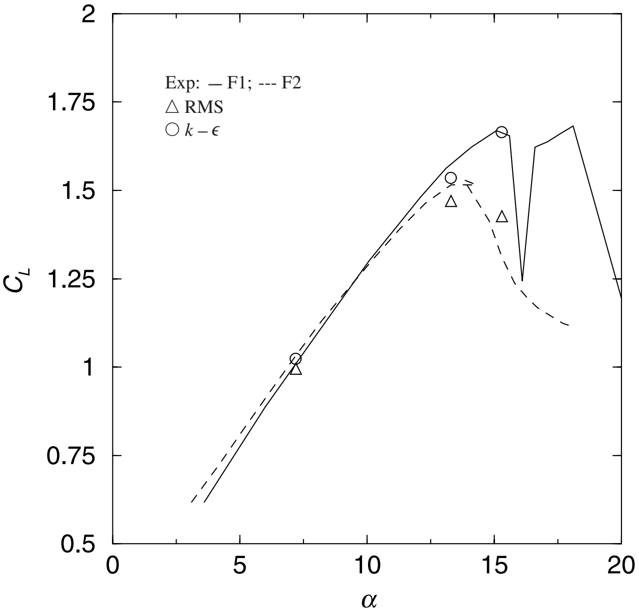

Fig. 4 Lift coefficient vs incidence angle α.

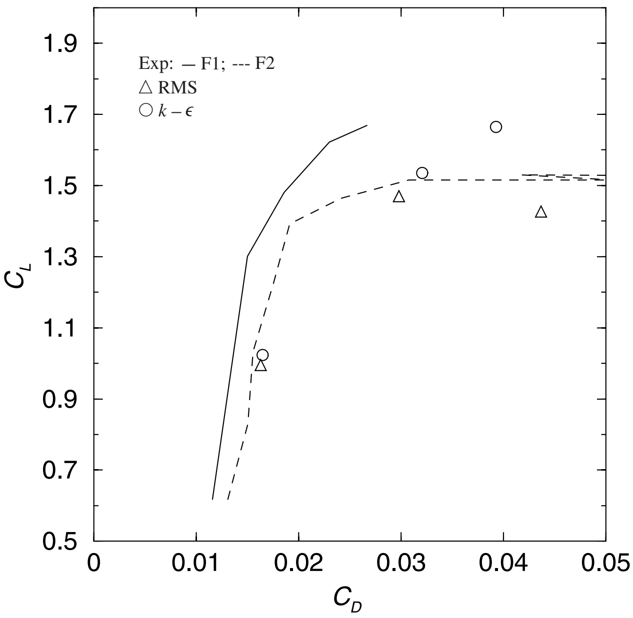

Fig. 5 Lift coefficient vs drag coefficient.

Results for *A*-airfoil with Attached Boundary Layer at 7.2 deg Angle of Attack

Friction and Pressure Coefficients

Figure 6 shows the evolution of the friction coefficient $C_f = \tau_w/0.5\rho_\infty u_\infty^2$ where τ_w is the shear stress on the suction side for both RSM and $k - \epsilon$ models. The rapid variation of this coefficient indicates the transition location of the flow. Then a regular diminution of the friction is observed until the trailing edge. As it is shown, a very good agreement is obtained between the RSM computation and the experimental data. The $k - \epsilon$ computation overpredicts the friction coefficient especially in the trailing edge region. This figure also reveals that the $k - \epsilon$ model slightly

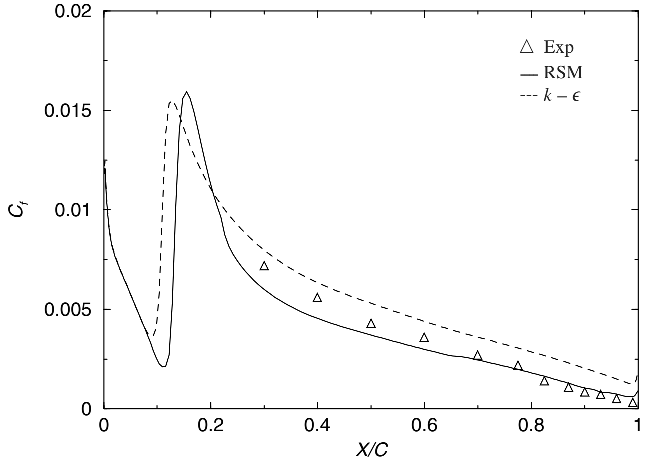

Fig. 6 Friction coefficient $C_f = \tau_w/(0.5\rho_\infty u_\infty^2)$ on the suction side; $\alpha = 7.2$ deg.

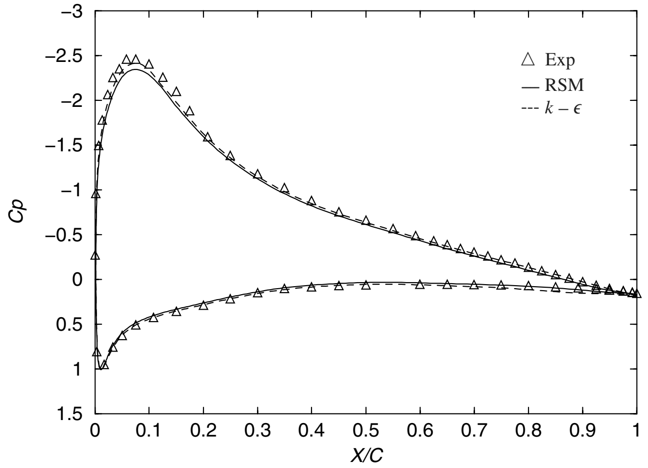

Fig. 7 Pressure coefficient $C_p = (p - p_\infty)/(0.5\rho_\infty u_\infty^2)$ around the airfoil; $\alpha = 7.2$ deg.

anticipates the transition location. Figure 7 describes the variation of the wall pressure coefficient $C_p = (p - p_\infty)/0.5\rho_\infty u_\infty^2$ on the suction and pressure sides of the airfoil. Fairly good agreements with the experimental data are observed for both turbulence models.

Velocity and Turbulent Profiles

More local details of the flow can be investigated through the velocity and turbulent stresses. Figure 8 displays the streamwise mean velocity profiles u_1/u_∞ vs the normal direction to the chordline of the wall at six locations on the suction side $x/c = 0.5$, 0.7, 0.825, 0.87, 0.93, and 0.99. For both turbulence models, the shape of the mean velocity profiles agrees rather well with the measurements although the thickness of the boundary layer for the $k-\epsilon$ computation is slightly overpredicted for the rear stations. The profiles of the streamwise turbulence stress τ_{11}, the transverse normal stress τ_{22}, and the shear stress τ_{12} at the stations $x/c = 0.7$, 0.87, and 0.99 on the suction side are plotted on Figs. 9–11, respectively. A very good agreement with the experimental data is achieved for the RSM computation. As expected, the $k-\epsilon$ computation yields quasi-isotropic normal stresses $\tau_{11} \approx \tau_{22} \approx 2k/3$ because of the Boussinesq hypothesis. For both stations, it is found that the streamwise stress τ_{11} is slightly underpredicted whereas the transverse normal stress τ_{22} is overpredicted. However, it appears that both turbulence models return reasonably well the level of the turbulent shear stress. Therefore, for that airfoil flow subjected to 7.2 deg incidence angle where the boundary layer remains attached, these results suggest that the flow velocities are much more sensitized to the shear stress than to the normal stresses.

Results for *A*-airfoil with Detached Boundary Layer at 13.3 deg Angle of Attack

Friction and Pressure Coefficients

Figure 12 describes the evolution of the friction coefficient C_f on the suction side for both turbulence models. It can be seen that the RSM prediction agrees very well with the measurements. The negative values reached at $x/c \approx 0.1$ indicate the location of the laminar separation bubble. Then the slow and regular decrease of the friction coefficient reveals the turbulent flow separation that occurs near the trailing edge. This result of interest confirms that the resolving of the laminar bubble influences the flow evolution around the trailing edge. In contrast to the RSM computation, the $k-\epsilon$ computation yields inappropriate evolution of the friction coefficient. The $k-\epsilon$ model highly anticipates the transition location in the upstream direction in comparison with the experimental result ($x/c = 0.12$) and the friction coefficient exhibits an overshoot. Moreover, the friction coefficient remains positive whatever the location on the suction side. These results mean that the $k-\epsilon$ model is incapable of resolving the laminar separation bubble and predicting the turbulent separation near the trailing edge. Variations of the wall pressure coefficient C_p on the suction and pressure sides of the airfoil are plotted in Fig. 13. For the RSM computation, the leading edge pressure peak on the suction side in the region where the flow is laminar appears a little too low. However, the evolution of the pressure coefficient agrees very well with the experimental data near the trailing edge, confirming the flow separation. The $k-\epsilon$ computation describes better the pressure peak but slightly overpredicts the measurements on the suction side in the region that extends from the transition location to the trailing edge.

Velocity and Turbulent Profiles

Investigations of the velocity and the turbulent stresses are worked out at several locations. Figure 14 shows the velocity profiles at six locations on the suction side $x/c = 0.5$, 0.7, 0.825, 0.87, 0.93, and 0.99. This figure indicates that the boundary layer is attached at $x/c = 0.5$. The inflexion in the velocity profile occurs between the location $x/c = 0.7$ and $x/c = 0.825$. Then, the boundary layer detaches from the airfoil near the trailing edge. Although this flow presents complex physics, one can notice that the RSM model predicts the velocity profiles in very good agreement with the measurements, whatever the development of the boundary layer, if attached or detached. Indeed, the inner boundary layer is decelerating at the correct rate, so that the boundary layer displacement thickness is well estimated by the RSM computation. On the contrary, the $k-\epsilon$ computation yields attached boundary layer whatever the location on the suction side. At $x/c = 0.5$, the boundary layer is near equilibrium and the $k-\epsilon$ velocity profile agrees with the measurements. But when increasing x/c, the velocity profiles highly deviate from the measurements and the boundary layer thickness is underpredicted. Such differences originate from the $k-\epsilon$ model which produces too high turbulence intensities. Indeed, Figs. 15–17 display the turbulent stress profiles on the suction side at the stations $x/c = 0.7$, 0.87, and 0.99. A first observation reveals that the RSM computation is still able to provide quantitative results compared with the experimental results. At the location $x/c = 0.7$, where the boundary layer is attached, the normal stresses and the shear stress agree very well with the measurements. At the other locations, where the boundary layer is detached, the profiles of the transverse normal stress τ_{22} and the shear stress τ_{12} follow rather well the experimental profiles, but the intensity of the streamwise stress τ_{11} is slightly underpredicted. As expected, the $k-\epsilon$ computation yields erroneous, almost isotropic, normal turbulent stresses τ_{11} and τ_{22}. At each location, the streamwise stress τ_{11} is underpredicted whereas the transverse normal stress τ_{22} is overpredicted (by about 50% at the station $x/c = 0.7$). Regarding the shear stress, it is surprising, however, that the intensity level is relatively well predicted except for the last station $x/c = 0.99$, where high discrepancies with the experimental

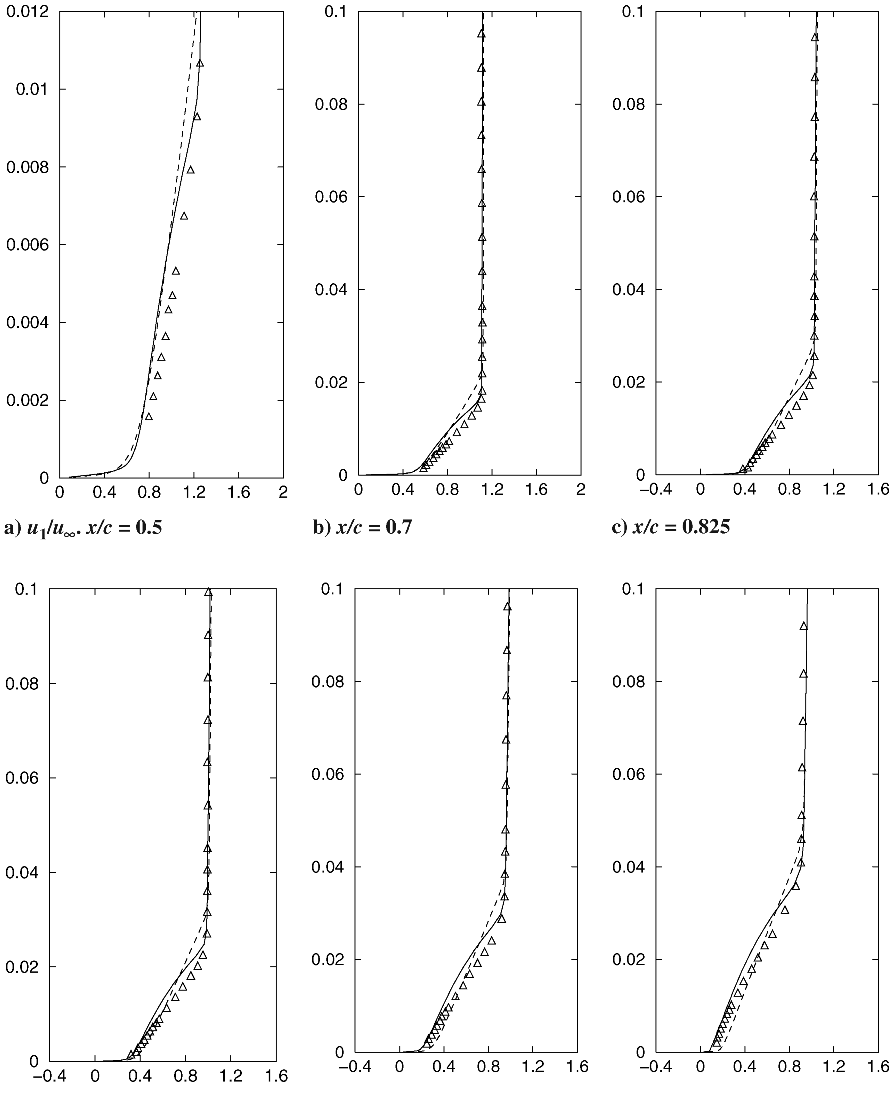
a) u_1/u_∞. $x/c = 0.5$
b) $x/c = 0.7$
c) $x/c = 0.825$
d) $x/c = 0.87$
e) $x/c = 0.93$
f) $x/c = 0.99$

Fig. 8 Velocity profiles u_1/u_∞ on the suction side: △ Exp; — RSM; -- $k - \epsilon$; $\alpha = 7.2$ deg.

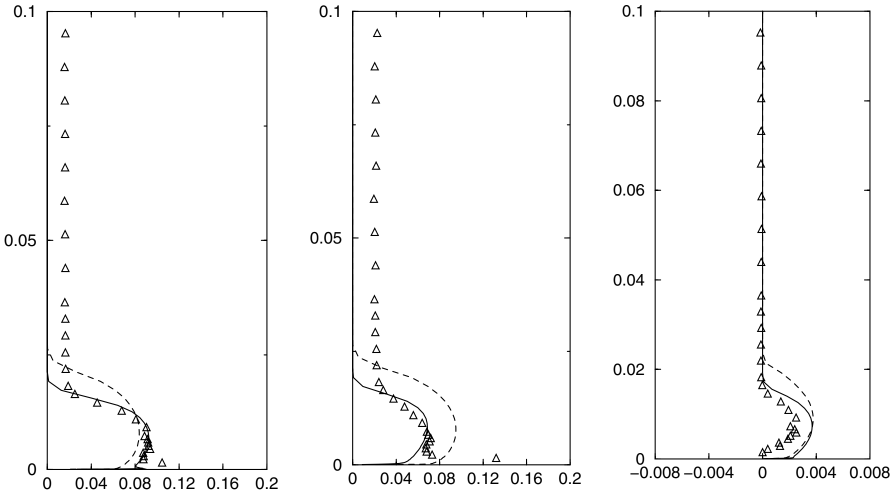
a) $\sqrt{\tau_{11}}/u_\infty$ $x/c = 0.7$
b) $\sqrt{\tau_{22}}/u_\infty$ $x/c = 0.7$
c) τ_{12}/u_∞^2 $x/c = 0.7$

Fig. 9 Turbulent stress profiles on the suction side: △ Exp; — RSM; -- $k - \epsilon$; $\alpha = 7.2$ deg.

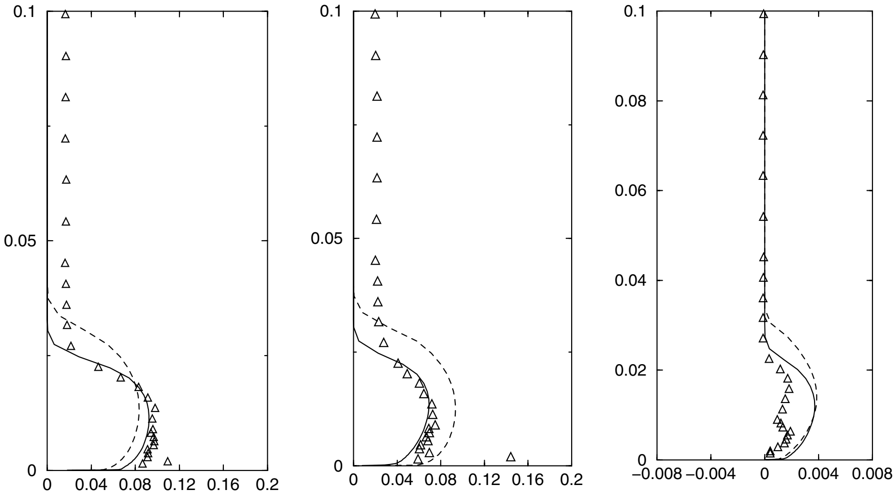

a) $\sqrt{\tau_{11}}/u_\infty$ $x/c = 0.87$ b) $\sqrt{\tau_{22}}/u_\infty$ $x/c = 0.87$ c) τ_{12}/u_∞^2 $x/c = 0.87$

Fig. 10 Turbulent stress profiles on the suction side: △ Exp; — RSM; -- $k-\epsilon$; $\alpha = 7.2$ deg.

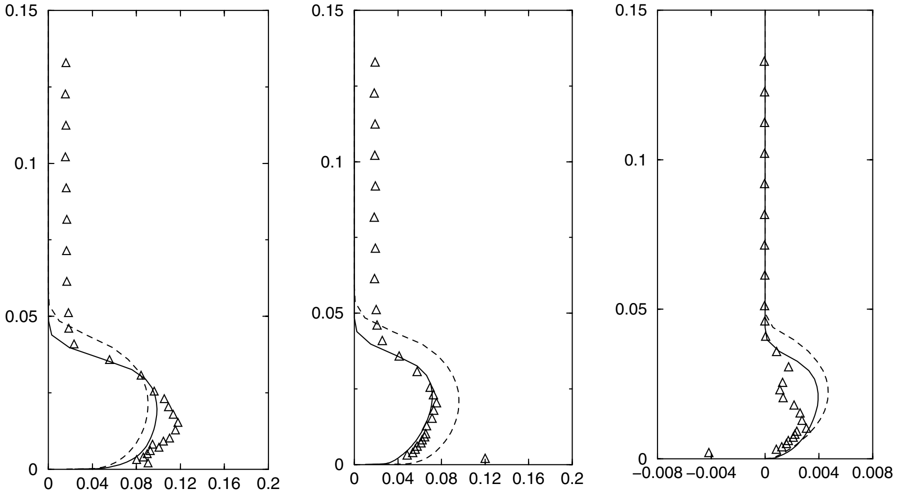

a) $\sqrt{\tau_{11}}/u_\infty$ $x/c = 0.99$ b) $\sqrt{\tau_{22}}/u_\infty$ $x/c = 0.99$ c) τ_{12}/u_∞^2 $x/c = 0.99$

Fig. 11 Turbulent stress profiles on the suction side: △ Exp; — RSM; -- $k-\epsilon$; $\alpha = 7.2$ deg.

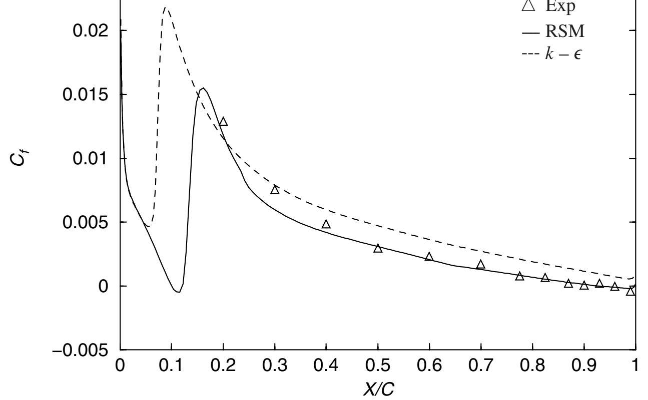

Fig. 12 Friction coefficient $C_f = \tau_w/(0.5\rho_\infty u_\infty^2)$ on the suction side; $\alpha = 13$ deg.

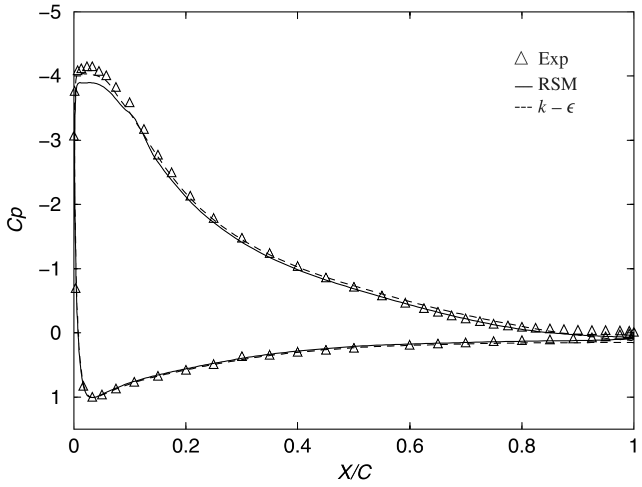

Fig. 13 Pressure coefficient $C_p = (p - p_\infty)/(0.5\rho_\infty u_\infty^2)$ around the airfoil; $\alpha = 13.3$ deg.

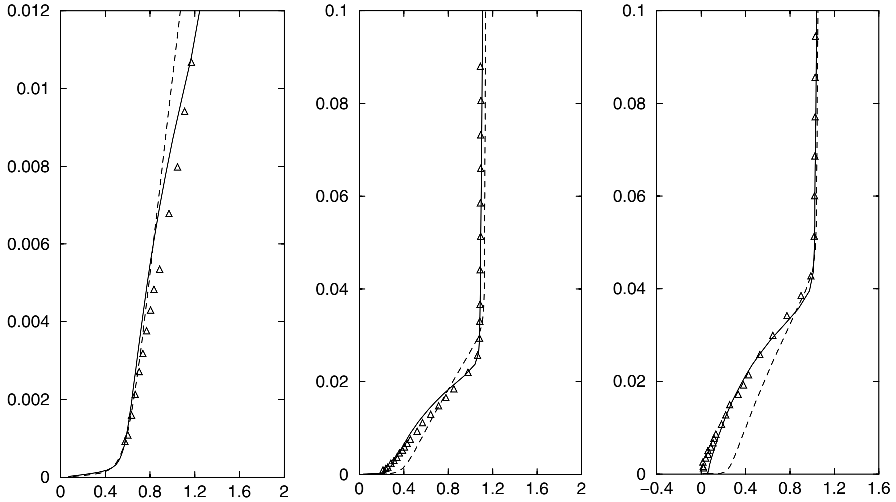

a) u_1/u_∞. $x/c = 0.5$ b) $x/c = 0.7$ c) $x/c = 0.825$

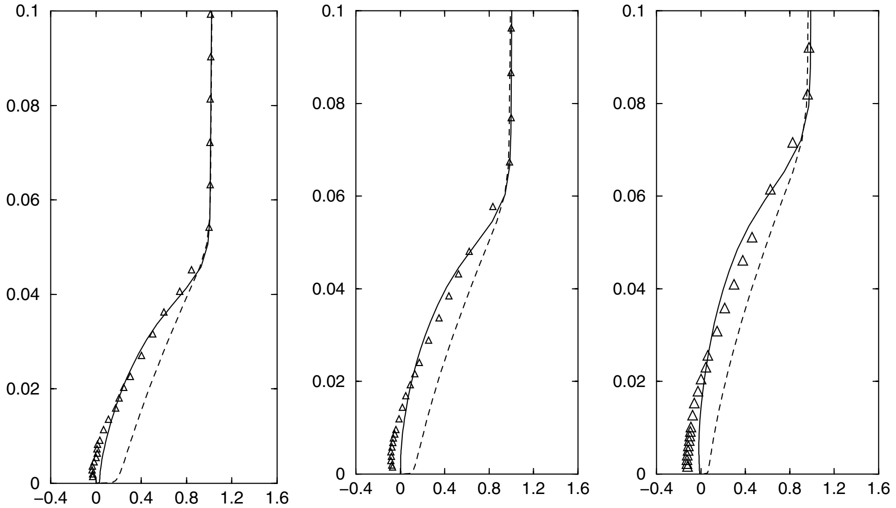

d) $x/c = 0.87$ e) $x/c = 0.93$ f) $x/c = 0.99$

Fig. 14 Velocity profiles u_1/u_∞ on the suction side: △ Exp; — RSM; -- $k-\epsilon$; $\alpha = 7.2$ deg.

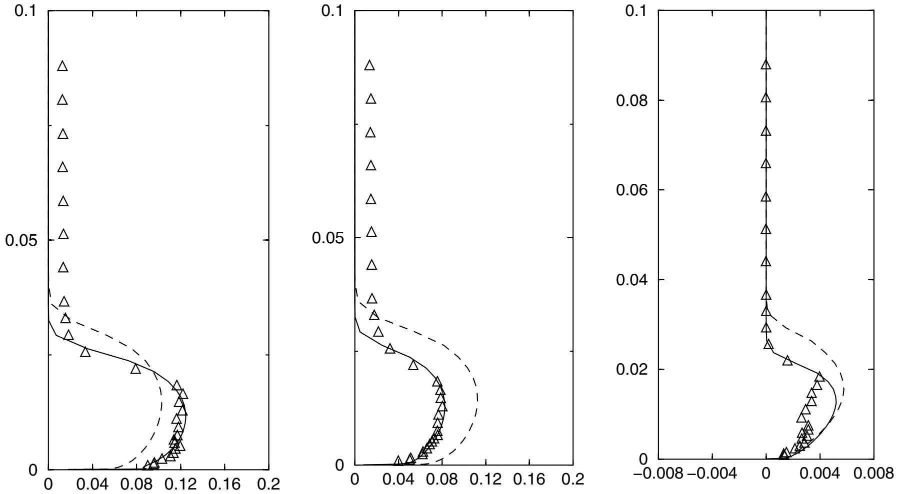

a) $\sqrt{\tau_{11}}/u_\infty$ $x/c = 0.7$ b) $\sqrt{\tau_{22}}/u_\infty$ $x/c = 0.7$ c) τ_{12}/u_∞^2 $x/c = 0.7$

Fig. 15 Turbulent stress profiles on the suction side: △ Exp; — RSM; -- $k-\epsilon$; $\alpha = 13.3$ deg.

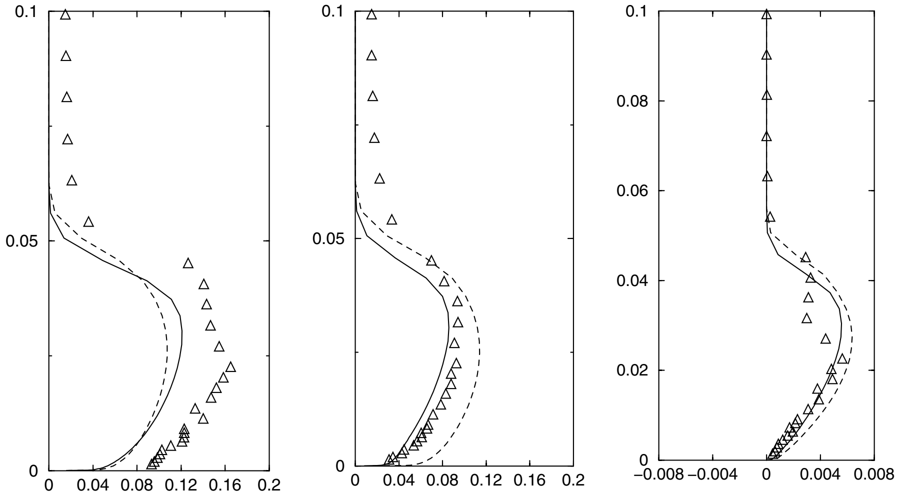

a) $\sqrt{\tau_{11}}/u_\infty$ $x/c = 0.87$ **b)** $\sqrt{\tau_{22}}/u_\infty$ $x/c = 0.87$ **c)** τ_{12}/u_∞^2 $x/c = 0.87$

Fig. 16 Turbulent stress profiles on the suction side: △ Exp; — RSM; -- $k-\epsilon$; $\alpha = 13.3$ deg.

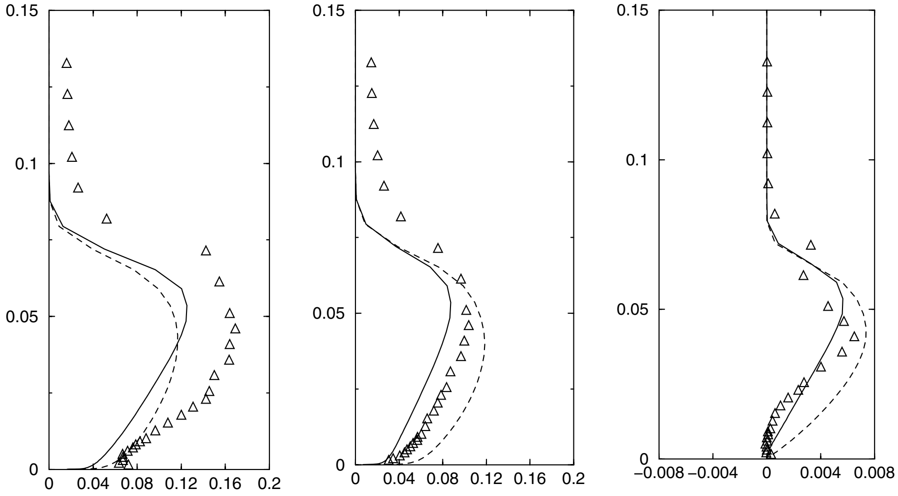

a) $\sqrt{\tau_{11}}/u_\infty$ $x/c = 0.99$ **b)** $\sqrt{\tau_{22}}/u_\infty$ $x/c = 0.99$ **c)** τ_{12}/u_∞^2 $x/c = 0.99$

Fig. 17 Turbulent stress profiles on the suction side: △ Exp; — RSM; -- $k-\epsilon$; $\alpha = 13.3$ deg.

data are observed. Lien and Leschziner [44] have mentioned in their work that the shear stress plays an important role in allowing the separation near the trailing edge. In the present case, it seems that the streamwise and transverse normal stresses also influence the flow separation. For instance, at the locations $x/c = 0.7$ and 0.87, the shear stresses produced by the $k-\epsilon$ and RSM computations are both close to the experimental data. The normal turbulent stresses of the RSM computation are well predicted but those of the $k-\epsilon$ computation present high discrepancies with the measurements. In that condition, one can reasonably assume that the differences in behavior of the $k-\epsilon$ and RSM velocity profiles are appreciably caused by the normal stresses that affect the motion through the averaged momentum Eq. (2). Comparisons with the previous airflow computation at 7.2 deg angle of attack show that the connection between the shear stress, the normal stresses, and the velocity is much more pronounced at high incidence angle than at low incidence.

In this work, the variant RSM model succeeds in producing the flow separation for two additional reasons. Firstly, it is able to take into account the flow anisotropy by redistributing the turbulent energy among the Reynolds stress components. Secondly, the function ψ_1 incorporated in the dissipation rate Eq. (15) is found to have significant effects in reducing the turbulence intensity where flows are far from equilibrium. This assertion can be easily demonstrated. When the production of the turbulent kinetic energy is much greater than the dissipation rate for nonequilibrium flows, the function ψ_1 in that case is positive because the flatness coefficient varies in the range domain between zero and unity. Therefore, the production of the dissipation rate $(c_{\epsilon_1} + \psi_1)\epsilon P_{mm}/2k$ in the ϵ transport equation is increased leading to an increase of the dissipation rate that has the effects of reducing all the turbulent stresses. Note that previous computations using the model of Launder and Shima [26] in its original form were not accurate because of the excessive value returned by the function ψ_1, provoking nonphysical flow relaminarization, as also observed for injection induced flows [28]. It is of interest to compare the present modeling and the SST correction used in two-equation models. In a preceding section, it has been recalled that the use of the eddy-viscosity limiter (SST) of Menter [18] consists in reducing the shear stress in boundary layer with adverse pressure gradient when the ratio of production to dissipation is significantly larger than one. This has a favorable effect in improving the tendency to flow separate, as observed by Larsson and Arlinger [45] performing $k-\omega/\epsilon$ A-airfoil flow computations. As a result, it is found that both the SST correction and the present modeled ϵ equation depend on the same quantity, which is the ratio of production to dissipation.

If improvement in the separation can be obtained for two-equation models with the SST correction, one has to keep in mind, however, that the normal turbulence stresses cannot be well-predicted using the Boussinesq hypothesis. In that situation, only appropriate RSM models or nonlinear models are able to predict both flow separation and fair anisotropic normal stresses.

Streamwise Velocity Contours

Figure 18 visualizes the streamwise velocity contours for both turbulence models. High resolution of the steady-state computational flowfield can be observed through the regular behavior of the contour lines. At the suction peak, the flow acceleration causes the laminar separation bubble followed by the transitional reattachment of the boundary layer. The development of the turbulent boundary layer, which results from the strong adverse pressure gradient, is also well-observed. The RSM computation yields a retarded boundary layer near the trailing edge according to the measurements, whereas those of the $k-\epsilon$ computation are too accelerated with no separation.

Streamline Contours

The streamline contours around the airfoil are shown in Fig. 19 for both RSM and $k-\epsilon$ computations. The separated flow is well-visible near the trailing edge leading to a decrease of the lift. This figure also confirms that the numerical scheme used in this application is quite appropriate. As already known, upwind schemes with high dissipation cannot describe accurately the separation flow region.

Turbulent Reynolds Number Contours

Figure 20 shows the contours of the turbulent Reynolds number $Re_t = k^2/\nu\epsilon$ for the RSM and $k-\epsilon$ computations. This figure shows clearly that the turbulence is more developed on the suction side for the $k-\epsilon$ computation than for the RSM computation, especially in the trailing edge region. According to the preceding discussion, one can also observe that the transition regime occurs earlier for the $k-\epsilon$ computation.

Results for A-airfoil with Detached Boundary Layer at 15.3 deg Angle of Attack

Streamline Contours

For that incidence angle, only the streamlines are visualized because of the lack of available measurements for the velocity and turbulent stresses. Figure 21 describes the streamline contours for both turbulence models. For the RSM computation, one can observe that a greater degree of separated flow is obtained at 15.3 deg than at 13.3 deg. These results indicate that the operating conditions of the airfoil are close to the static stall because of the massive separation that occurs near the trailing edge. Somewhat surprisingly, the boundary layer still remains attached for the $k-\epsilon$ computation even at 15.3 deg, leading to an overestimated lift. This result confirms that the standard $k-\epsilon$ model, known to be quite insensitive to adverse pressure gradient, is not appropriate for this type of flow, contrary to second-order models which are very promising.

Conclusions

A Reynolds stress transport modeling has been applied for attached and separated flows over a high-lift airfoil designed by Aérospatiale for several angles of incidence, 7.2, 13.3, and 15.3 deg.

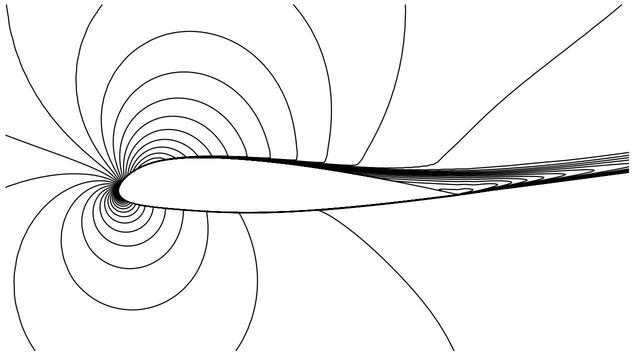

a) RSM computation. α=13.3 deg

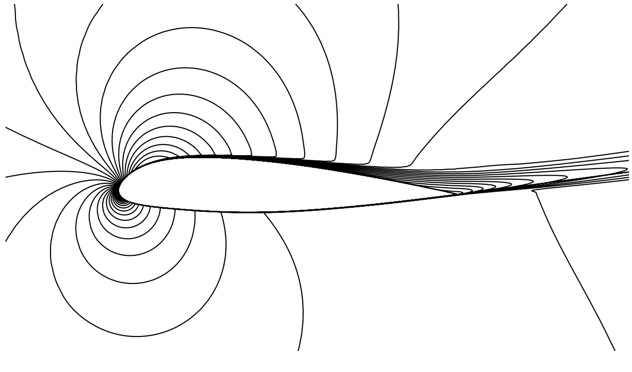

b) $\kappa-\varepsilon$ computation. α=13.3 deg

Fig. 18 Streamwise velocity contours.

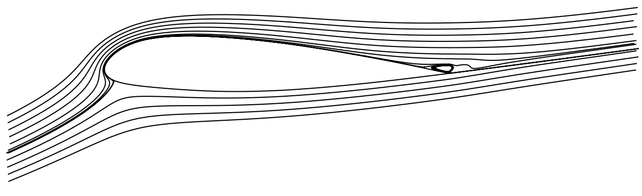

a) RSM computation. α=13.3 deg

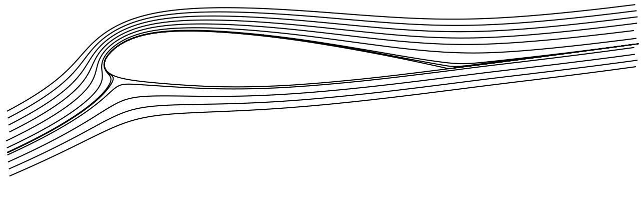

b) $\kappa-\varepsilon$ computation. α=13.3 deg

Fig. 19 Streamwise contours.

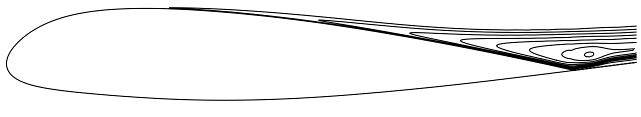

a) RSM computation. α=13.3 deg

b) $\kappa-\varepsilon$ computation. α=13.3 deg

Fig. 20 Contours of turbulent Reynolds number $Re_t = k^2/\nu\epsilon$; $\Delta = 100$.

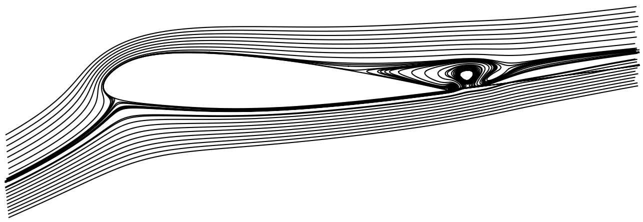

a) RSM computation. α =15.3 deg

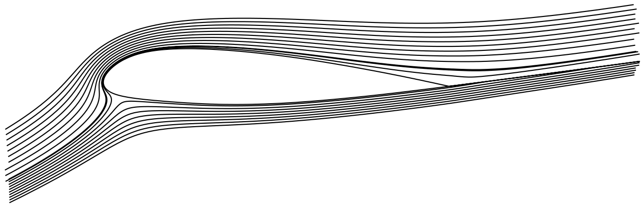

b) $\kappa - \varepsilon$ computation. α =15.3 deg

Fig. 21 Streamline contours.

In this work, a variant RSM model of Launder and Shima [26], taking into account some modifications and improvements, as well as the standard $k - \epsilon$ model of Launder and Sharma [27] have been used for comparison. It has been shown that the RSM model satisfies the weak form of the realizability conditions to ensure physical results. An accurate TVD scheme of high resolution has been considered for this application. As a result of computations, it is found that the variant RSM model, taking into account some improvements in comparison with standard models, predicts numerically these airfoil flows for a large range of incidences in a very good agreement with the experimental data. Particularly for the case 13.3 deg, the RSM computation is able to reproduce fairly well the laminar separation bubble, the transition, and the turbulent reattachment, as well as the turbulent separation. The separated flow which appears near the trailing edge is well-visible. Indeed, a theoretical analysis of second-moment modeling suggests that these flows are not only governed by the shear stress as usually observed at low incidence angle, but are also affected by the normal turbulent stresses, as well as by the ratio of production to dissipation in the boundary layer, at high incidence angle. As expected, the $k - \epsilon$ model [27] provides very poor performances near the static stall.

References

[1] Epstein, B., Rubin, T., and Seror, S., “Accurate Mutilblock Navier–Stokes Solver for Complex Aerodynamic Configurations,” *AIAA Journal*, Vol. 41, No. 4, 2003, pp. 582–594.

[2] Spalart, P. R., “Strategies for Turbulence Modeling and Simulations,” *International Journal of Heat and Fluid Flow*, Vol. 21, 2000, pp. 252–263.

[3] Rhie, C. M., and Chow, W. L., “Numerical Study of the Turbulent Flow Past an Airfoil Trailing Edge Separation,“ *AIAA Journal*, Vol. 21, No. 11, 1983, pp. 1525–1532.

[4] Rumsey, C. L., and Vasta, V. N., “Comparison of the Predictive Capabilities of Several Turbulence Models,” *Journal of Aircraft*, Vol. 32, No. 3, 1995, pp. 510–514.

[5] Chaouat, B., “Numerical Simulations of Fully Developed Channel Flows Using $k - \epsilon$, Algebraic, and Reynolds Stress Models,” *In 37th AIAA Aerospace Sciences Meeting and Exhibit*, AIAA Paper 99-0158, Jan. 1999.

[6] Rumsey, C. L., and Gatski, T. B., “Recent Turbulence Model Advances Applied to Multi-Element Airfoil Computations,” *Journal of Aircraft*, Vol. 38, No. 5, 2001, pp. 904–910.

[7] Launder, B. E., Reece, G. J., and Rodi, W., “Progress in the Development of a Reynolds Stress Turbulence Closure,” *Journal of Fluid Mechanics*, Vol. 68, No. 3, 1975, pp. 537–566.

[8] So, R. M. C., Lai, Y. G., and Zhang, H. S., “Second Order Near Wall Turbulence Closures: a Review,” *AIAA Journal*, Vol. 29, No. 11, 1991, pp. 1819–1835.

[9] Leschziner, M. A., “Computation on Aerodynamic Flows with Turbulence-Transport Models Based on Second-Moment Closure,” *Computers & Fluids*, Vol. 24, No. 4, 1995, pp. 377–392.

[10] Speziale, C. G., Sarkar, S., and Gatski, T. B., “Modeling the Pressure-Strain Correlation of Turbulence: an Invariant Dynamical Systems Approach,” *Journal of Fluid Mechanics*, Vol. 227, 1991, pp. 245–272.

[11] Gibson, M. M., and Launder, B. E., “Ground Effects on Pressure Fluctuations in the Atmospheric Boundary Layer,” *Journal of Fluid Mechanics*, Vol. 86, No. 3, 1978, pp. 491–511.

[12] Hanjalic, K., “Advanced Turbulence Closure Models: a View of Current Status and Future Prospects,” *International Journal of Heat and Fluid Flow*, Vol. 15, No. 3, 1994, pp. 178–203.

[13] So, R. M. C., and Yuan, Y. G., “A Geometry Independent Near-Wall Reynolds-Stress Closure,” *International Journal of Engineering Science*, Vol. 37, 1999, pp. 33–57.

[14] Batten, P., Craft, T. J., Leschziner, M. A., and Loyau, H., “Reynolds-Stress Transport Modeling for Compressible Aerodynamics Applications,” *AIAA Journal*, Vol. 37, No. 7, 1999, pp. 785–797.

[15] Gerolymos, G. A., Sauret, E., and Vallet, I., “Contribution to Single-Point Closure Reynolds-Stress Modeling of Inhomogeneous Flow,” *Theoretical and Computational Fluid Dynamics*, Vol. 17, 2004, pp. 407–431.

[16] Haase, W., Chaput, E., Elsholz, E., Leschziner, E., and Muller, M., *ECARP-European Computational Aerodynamics Research Project: Validation of CFD Code and Assessment of Turbulence Models*, Vieweg, Brunswick, Germany, 1997.

[17] Menter, F. R., “Performance of Popular Turbulence Models for Attached and Separated Adverse Pressure Gradient Flows,” *AIAA Journal*, Vol. 30, No. 8, 1992, pp. 2066–2072.

[18] Menter, F. R., “Two-Equations Eddy-Viscosity Turbulence Models for Engineering Applications,” *AIAA Journal*, Vol. 32, No. 8, 1994, pp. 1598–1605.

[19] Davidson, L., Cokljat, D., Frohlich, J., Leschziner, M., Meelen, C., and Rodi, W., *LESFOIL: Large Eddy Simulation of Flow Around a High Lift Airfoil*, Springer, New York, 2003.

[20] Mellen, P., Frohlich, J., and Rodi, W., “Lessons from LESFOIL Project on Large-Eddy Simulation of Flow Around an Airfoil,” *AIAA Journal*, Vol. 41, No. 4, 2003, pp. 573–581.

[21] Schiestel, R., and Dejoan, A., “Towards a New Partially Integrated Transport Model for Coarse Grid and Unsteady Turbulent Flow Simulations,” *Theoretical and Computational Fluid Dynamics*, Vol. 18, 2005, pp. 443–468.

[22] Chaouat, B., and Schiestel, R., “A New Partially Integrated Transport Model for Subgrid-Scale Stresses and Dissipation Rate for Turbulent Developing Flows,” *Physics of Fluids*, Vol. 17, No. 6, 2005.

[23] Chaouat, B., and Schiestel, R., Progress in Subgrid-Scale Transport Modeling Using Partial Integration Method for LES of Developing Turbulent Flows*Direct and Large Eddy Simulation 6*, edited by E. Lamballais, R. Friedrich, B. Geurts, and O. Metais, Vol. 10, European Research Community on Fluids, Turbulence and Combustion Series, Springer, 2006.

[24] Leschziner, M. A., and Drikakis, D., “Turbulence Modeling and Turbulent-Flow Computation in Aeronautics,” *The Aeronautical Journal*, Vol. 106, 2002, pp. 349–384.

[25] Leschziner, M. A., “Turbulence Modeling for Separated Flows with Anisotropy-Resolving Closures,” *Philosophical Transactions of the Royal Society of London, Series A: Mathematical and Physical Sciences*, Vol. 358, 2000, pp. 3247–3277.

[26] Launder, B. E., and Shima, N., “Second Moment Closure for the Near Wall Sublayer: Development and Application,” *AIAA Journal*, Vol. 27, No. 10, 1989, pp. 1319–1325.

[27] Launder, B. E., and Sharma, B., “Application of the Energy Dissipation Model of Turbulence to the Calculation of Flow Near a Spinning Disc,” *Letters in Heat and Mass Transfer*, Vol. 1, 1974, pp. 131–138.

[28] Chaouat, B., “Simulations of Channel Flows with Effects of Spanwise Rotation or Wall Injection Using a Reynolds Stress Model,” *Journal of Fluids Engineering*, American Society of Mechanical Engineers, Vol. 123, March 2001, pp. 2–10.

[29] Hanjalic, K., Hadzic, L., and Jakirlic, S., “Modeling Turbulent Wall Flows Subjected to Strong Pressure Variations,” *Journal of Fluids Engineering*, American Society of Mechanical Engineers, Vol. 121, March 1999, pp. 57–64.

[30] Crow, S. C., “Viscoelastic Properties of the Fine-Grained Incompressible Turbulence,” *Journal of Fluid Mechanics*, Vol. 33, No. 1, 1968, pp. 1–20.

[31] Daly, B. J., and Harlow, F. H., “Transport Equations in Turbulence,” *Physics of Fluids*, Vol. 13, No. 11, 1970, pp. 2634–2649.

[32] Craft, T. J., “Developments in a Low-Reynolds Number Second-

Moment Closure and its Application to Separating and Reattaching Flows," *International Journal of Heat and Fluid Flow*, Vol. 19, 1998, pp. 541–548.

[33] Hanjalic, K., and Launder, B. E., "Contribution Toward a Reynolds-Stress Closure for Low-Reynolds-Numbers Turbulence," *Journal of Fluid Mechanics*, Vol. 74, No. 4, 1976, pp. 593–610.

[34] Chaouat, B., "Numerical Predictions of Channel Flows with Fluid Injection Using Reynolds Stress Model," *Journal of Propulsion and Power*, Vol. 18, No. 2, 2002, pp. 295–303.

[35] Gerolymos, G. A., and Vallet, I., "Wall-Normal-Free Reynolds-Stress Closure for Three-Dimensional Compressible Separated Flows," *AIAA Journal*, Vol. 39, No. 10, 2001, pp. 1833–1841.

[36] Schumann, U., "Realizability of Reynolds Stress Turbulence Models," *Physics of Fluids*, Vol. 20, No. 5, 1977, pp. 721–725.

[37] Speziale, C. G., Abid, R., and Durbin, P. A., "On the Realisability of Reynolds Stress Turbulence Closures," *Journal of Scientific Computing*, Vol. 9, No. 4, 1994, pp. 369–403.

[38] Chaouat, B., "Simulations Numériques d'Ecoulements Pleinement Développés dans un Canal Plan par des Modèles du Premier Ordre $k - \epsilon$ et du Second Ordre aux Tensions de Reynolds, RSM," ONERA RTS 23/1145, 1998.

[39] Roe, P. L., "Approximate Riemann Solvers, Parameter Vectors and Difference Schemes," *Journal of Computational Physics*, Vol. 43, 1981, pp. 357–372.

[40] Dutoya, D., and Errera, M. P., "A Formal Decomposition of the Jacobian Matrix of the Euler Equations. Application to Upwind Numerical Schemes." *La Recherche Aérospatiale : Bulletin Bimestriel De L'office National D'études et de Recherches Aérospatiales*, Vol. 1, 1992, pp. 25–35.

[41] Chaouat, B., and Schiestel, R., "Reynolds Stress Transport Modeling for Steady and Unsteady Channel Flows with Wall Injection," *Journal of Turbulence*, Vol. 3, 2002, pp. 1–15.

[42] Houddeville, R., Piccin, O., and Cassoudesalle, D., "Opération Décrochage à la Souflerie Fl," ONERA RT OA 19/5025, 1987.

[43] Gleize, C., "Opération Décrochage. Résultats des Essais à la Souflerie F2," ONERA RT OA 55/4004, 1988.

[44] Lien, F. S., and Leschziner, M. A., "Modeling 2D Separation from a High Lift Aerofoil with a Non-Linear Eddy Viscosity Model and Second-Moment Closure," *The Aeronautical Journal*, Vol. 99, 1995, pp. 125–143.

[45] Larsson, T., and Arlinger, B. G., *On the Prediction of Flows Around Airfoils at High Lift Conditions, in ECARP-European Computational Aerodynamics Research Project*, edited by Haase, W., Chaput, E., Elsholz, E., Leschziner, E., and Muller, M., Vieweg, Brunswick, Germany, 1997, pp. 241–252.

R. M. C. So
Associate Editor